Available online at www.sciencedirect.com
ScienceDirect
Comput. Methods Appl. Mech. Engrg. 372 (2020) 113394
Computer methods in applied mechanics and engineering
www.elsevier.com/locate/cma

Curvilinear virtual elements for contact mechanics

Fadi Aldakheel[a,*], Blaž Hudobivnik[a], Edoardo Artioli[b], Lourenço Beirão da Veiga[c], Peter Wriggers[a]

[a] Institute of Continuum Mechanics (IKM), Leibniz Universität Hannover (LUH), An der Universität 1, 30823 Garbsen, Germany
[b] Department of Civil Engineering and Computer Science, University of Rome Tor Vergata, Via del Politecnico 1, 00133 Roma, Italy
[c] Department of Mathematics and Applications, University of Milano-Bicocca, Via R. Cozzi 55, 20125 Milano, Italy

Received 24 April 2020; received in revised form 21 August 2020; accepted 21 August 2020
Available online 8 September 2020

Abstract

The virtual element method (VEM) for curved edges with applications to contact mechanics is outlined within this work. VEM allows the use of non-matching meshes at interfaces with the advantage that these can be mapped to a simple node-to-node contact formulation. To account for exact approximation of complex geometries at interfaces, we developed a VEM technology for contact that considers curved edges. A number of numerical examples illustrate the robustness and accuracy of this discretization technique. The results are very promising and underline the advantages of the new VEM formulation for contact between two elastic bodies in the presence of curved interfaces.

Keywords: Virtual element method (VEM); Curved edges; Contact discretization; Non-conforming mesh

1. Introduction

Many techniques were developed over the years to formulate constraints at contact interfaces between bodies in computational contact mechanics. In finite element (FEM) approach the method of Lagrange multipliers, the penalty method or other techniques like the augmented Lagrangian formulation or barrier techniques were implemented to design robust and efficient contact algorithms. An overview is provided in the textbooks of [1,2].

A great number of numerically motivated approaches to discretize the contact area can be found in the literature. Classical studies of [3–5] on contact discretizations are based on nodal enforcement of the constraints. To improve the robustness of solution schemes the interpolation was enhanced in [6–9] to reach C^1-continuity. This leads to a continuous and smooth field of the normal vector. Isogeometric formulations enhance the contact surface quality, as discussed in the works [10–13]. Nevertheless such contact formulations still need high implementation efforts. Mortar methods provide a continuous discretization of the contact interface as outlined in [14–21]. Hereby, the mortar domain represents both non-matching sides exactly. However, the additional discretization of non-matching surface patches adds to the complexity of the implementation.

A relatively new method – the virtual element method (VEM) – will be presented in this contribution that leads to an exceptional efficient and stable formulation for non-matching contact interfaces. The method was firstly

* Corresponding author.
E-mail addresses: aldakheel@ikm.uni-hannover.de (F. Aldakheel), hudobivnik@ikm.uni-hannover.de (B. Hudobivnik), artioli@ing.uniroma2.it (E. Artioli), lourenco.beirao@unimib.it (L. Beirão da Veiga), wriggers@ikm.uni-hannover.de (P. Wriggers).

https://doi.org/10.1016/j.cma.2020.113394

developed by F. Brezzi, L. Beirao da Veiga and coworkers, see [22,23]. The advantage of the virtual element method is that different numbers of nodes can be used to define an element. This characteristic fits extremely well into a general contact formulation with non-matching meshes, since it allows to add additional nodes on the fly and thus to formulate a node-to-node contact approach. VEM has been developed over the last seven years and applied to various problems in solid and fluid mechanics, an overview can be found in [24]. Limiting ourselves to the solid mechanics literature, recent works on virtual elements have been devoted to linear elasticity in [25–28], contact problems in [29,30], elasto-plasticity in [31–33], anisotropic materials in [34,35], curvilinear virtual elements for 2D solid mechanics applications in [36], hyperelastic materials at finite deformations in [37,38], fracture mechanics in [39–43], topology optimization in [44], vibration problems in [45–47], asymptotic homogenization in [48] and general element shapes in [49].

In this work, we extend the VEM technology for contact described in [29] towards curved edges/faces. The additional important feature (i.e. that the virtual elements are allowed to exhibit curved edges) leads to an exact approximation of the geometry, as well documented in [36,50,51]. It turns out that in the presence of curved geometries these new virtual elements are the natural choice also for problems in contact mechanics. This is due to promising results which underline the advantages of the curved VEM approach over the standard one. In this contribution the augmented Lagrangian formulation is used to describe the contact constrains. Such methodology is flexible and provides good algorithmic convergence properties as outlined in [6,52].

Two discretization strategies will be pursued in this contribution to compare the new VEM formulations with the standard FEM: (i) Node-On-Segment, suitable for both FEM and VEM and (ii) Node-on-Node, where the advantage of VEM can be utilized for non-matching meshes at the contact interface. Moreover, the above VEM study cases will be analyzed for two stabilization types: sub-triangulation (Stab. A) introduced in [38]; and algebraic stabilization (Stab. B) developed in [22,27]. Another important aspect of this work is the development of locally refined meshes for VEM, which produces accurate and more stable results than fully refined Voronoi or triangular meshes. Furthermore this refinement strategy reduces the number of total degrees of freedom, thus decreasing the computation time.

The paper is organized as follows. In Section 2 the governing equations for contact problem between two elastic bodies are outlined. Section 3 summaries the curvilinear virtual element formulations. It includes details on the two important stabilization schemes of VEM. Afterward, we describe the contact discretization strategies in Section 4. To verify the proposed virtual element formulations with curved edges, a number of examples in Section 5 are demonstrated and discussed. Section 6 briefly summarizes the work and gives some concluding remarks.

2. Governing equations

The contacting continua are chosen as linear elastic bodies occupying bounded domains $\Omega^\alpha\,(\alpha = 1, 2) \subset \mathbb{R}$. The boundary-value-problem (BVP) is characterized at material points $\boldsymbol{x} \in \Omega^\alpha$ and time t by the displacement field $\boldsymbol{u}^\alpha(\boldsymbol{x}, t)$ in a small strain setting. The gradient of the displacement field defines the symmetric strain tensor of the geometrically linear theory

$$\boldsymbol{\varepsilon}^\alpha = \nabla_s \boldsymbol{u}^\alpha = \mathrm{sym}[\nabla \boldsymbol{u}^\alpha] := \frac{1}{2}[\nabla \boldsymbol{u}^\alpha + \nabla \boldsymbol{u}^{\alpha\,T}] \,. \tag{1}$$

For the construction of a BVP boundary condition, balance and constitutive equations have to be formulated. The boundaries Γ_i of the two elastic bodies in Fig. 1 are decomposed into Dirichlet Γ_{D^α}, Neumann Γ_N^α and contact Γ_C parts. The Dirichlet and Neumann boundary conditions are defined as

$$\boldsymbol{u}^\alpha = \bar{\boldsymbol{u}}^\alpha \quad \text{on } \Gamma_D^\alpha \qquad \text{and} \qquad \boldsymbol{t}^\alpha = \bar{\boldsymbol{t}}^\alpha \quad \text{on } \Gamma_N^\alpha \qquad \text{with} \qquad \boldsymbol{t}^\alpha = \boldsymbol{\sigma}^\alpha \boldsymbol{n}^\alpha \tag{2}$$

in terms of the prescribed displacement $\bar{\boldsymbol{u}}^\alpha$ and surface traction $\bar{\boldsymbol{t}}$, the symmetric Cauchy stress tensor $\boldsymbol{\sigma}^\alpha$, the surface normal vector $\boldsymbol{n}^\alpha$ and traction $\boldsymbol{t}^\alpha$ related to body Ω^α.

The contact boundary Γ_C is considered as a priori unknown area where the two elastic bodies come in contact, as visualized in Fig. 1.

Both bodies have to satisfy the equation of equilibrium on Ω^1 and Ω^2, respectively, as

$$\boxed{\mathrm{div}\,\boldsymbol{\sigma}^\alpha + \bar{\boldsymbol{f}}^\alpha = \boldsymbol{0}} \tag{3}$$

where dynamic effects are neglected and $\bar{\boldsymbol{f}}$ is the given body force.

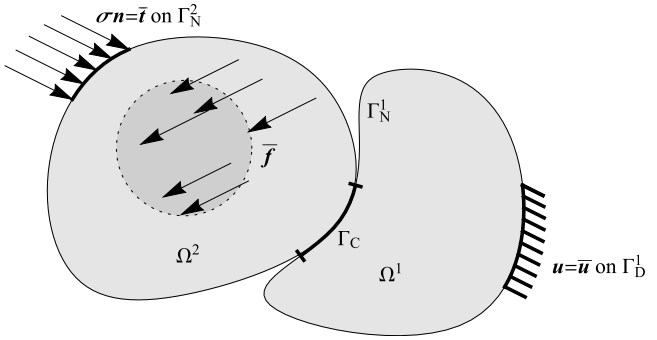

Fig. 1. Two continuum bodies Ω^1 and Ω^2 in contact. Additional to the Neumann and Dirichlet boundaries there also is a contact partition Γ_C of the boundary.

The stresses in Ω^1 and Ω^2 are obtained from the strain energy function $\Psi(\boldsymbol{u})$ following the Coleman–Noll procedure as

$$\boldsymbol{\sigma}^\alpha = \frac{\partial \Psi^\alpha(\boldsymbol{\varepsilon})}{\partial \boldsymbol{\varepsilon}}\,, \tag{4}$$

here the stress tensor $\boldsymbol{\sigma}^\alpha$ is the thermodynamic dual to $\boldsymbol{\varepsilon}^\alpha$. For a homogeneous isotropic elastic material, the strain energy function for the body Ω^α is given by

$$\Psi^\alpha = \frac{\lambda}{2}\,\mathrm{tr}^2[\boldsymbol{\varepsilon}] + \mu\,\mathrm{tr}[\boldsymbol{\varepsilon}^2], \tag{5}$$

with the two Lamé constants λ and μ defined in terms of elastic Young's modulus and Poisson's ratio as

$$\lambda := \frac{E\nu}{(1+\nu)(1-2\nu)} \qquad \text{and} \qquad \mu := \frac{E}{2(1+\nu)}\,. \tag{6}$$

An equivalent setting to the strong formulation in (3) is using the potential energy $U^\alpha(\boldsymbol{u})$. Its variation yields the equilibrium conditions. Such a choice is often utilized as a basis for the derivation of a discretization scheme and will here also be applied for the virtual element method. For the contact problem between two elastic bodies in (5) the potential energy function is given by

$$U(\boldsymbol{u}) = \sum_{\alpha=1}^{2} \left[\int_{\Omega^\alpha} [\,\Psi^\alpha(\boldsymbol{u}^\alpha) - \bar{\boldsymbol{f}}^\alpha \cdot \boldsymbol{u}^\alpha]\, d\Omega^\alpha - \int_{\Gamma_N^\alpha} \bar{\boldsymbol{t}}^\alpha \cdot \boldsymbol{u}^\alpha\, d\Gamma^\alpha \right] + U_c\,. \tag{7}$$

Here the part U_c is the contribution due to contact constraints.

The contact conditions can be defined by looking at the gap between the two surfaces of bodies Ω^α. This gap is given by

$$g_n = (\boldsymbol{u}^2 - \boldsymbol{u}^1)\cdot \boldsymbol{n}^1 + g_0 \tag{8}$$

as the normal distance between the bodies. In this relation $\boldsymbol{n}^1$ is the surface normal related to one of the bodies and g_0 is the initial gap between the bodies. Since no adhesion forces are allowed at the contact interface the normal stress σ_n has to be negative. On the other hand, no penetration is allowed. Both conditions can be cast in the so called Karush–Kuhn–Tucker (KKT) conditions, see e.g. [1],

$$g_n \geq 0, \quad \sigma_n \leq 0 \quad \text{and} \quad g_n\,\sigma_n = 0\,. \tag{9}$$

where $\sigma_n = \boldsymbol{t}^1 \cdot \boldsymbol{n}^1 = -\boldsymbol{t}^2 \cdot \boldsymbol{n}^2$ is the normal contact stress exerted due to action/reaction at the contact interface. The first of the KKT inequalities is related to the non-penetration; the second KKT inequality states that the contact stress is always negative; and the third condition takes care of the fact that the gap and normal stress cannot be non-zero at the same time.

Classically the above KKT relations lead to a variational inequality. This inequality is usually solved by an active set method that assumes for a given part of the boundary an existing contact, defined as contact interface. At this

interface the gap between both bodies is zero which introduces a constraint in the formulation. This can be included in the variational formulation (7) by a special form of U_c. Common formulations are provided by the method of Lagrange multipliers, the penalty method, combined techniques like the augmented Lagrangian formulation or barrier techniques, for details see [1].

Since the augmented Lagrangian formulation is most flexible and provides good algorithmic convergence properties, see e.g. [6] and [52], it is used here. The energy U_c contributing to (7) is then given by

$$U_c = \begin{cases} \int_{\Gamma_C} (\lambda_n + \frac{\epsilon_n}{2} g_n) g_n \, d\Gamma & \text{for} \quad \lambda_n \leq 0 \quad \text{(contact)} \\ -\int_{\Gamma_C} \frac{1}{2\epsilon_n} \lambda_n^2 \, d\Gamma & \text{for} \quad \lambda_n > 0 \quad \text{(separation)} \end{cases} \tag{10}$$

with the Lagrangian multiplier λ_n and the penalty parameter ϵ_n. Here we assume frictionless contact. Thus there is no contribution in tangential direction within the contact interface. Hence neither stick nor frictional sliding is considered. The formulation (10) yields a C^1-continuous saddle point functional, for details see [6].

It is easy to see that this augmented Lagrangian formulation is a combination of the Lagrangian multiplier methods which would lead to

$$U_c^{LM} = \begin{cases} \int_{\Gamma_C} \lambda_n \, g_n \, d\Gamma & \text{for} \quad g_n \leq 0 \\ 0 & \text{for} \quad g_n > 0 \end{cases} \tag{11}$$

and the penalty formulation which would contribute to (7) by

$$U_c^{P} = \begin{cases} \frac{1}{2} \int_{\Gamma_C} \epsilon_n \, g_n^2 \, d\Gamma & \text{for} \quad g_n \leq 0 \\ 0 & \text{for} \quad g_n > 0 \end{cases} \tag{12}$$

with the contact penalty parameter ϵ_n for the normal direction.

3. Formulation of the virtual element method

The virtual element method (VEM) offers an element formulation for a mesh of polygons with a variable number of nodes, as outlined in [22,23,27,41]. This is possible by choosing the ansatz space directly in the physical domain and allowing for functions that are non-polynomial.

In the present section we describe the Virtual Element Method for (two dimensional) small deformation solid mechanics problems, with the additional important feature that the mesh elements are allowed to exhibit curved edges. The involved spaces and construction were introduced in [50] and further developed in [36,51]. We here limit the description to the lowest order case (that is the "linear" element) and refer to the above papers for the higher order case.

3.1. The local VEM space

In standard first-order finite elements, the local "linear" displacement space makes use of 6 degrees of freedom, given by the three (vector-valued) evaluations at the vertices of the triangle. The present more general construction keeps the same simple degrees of freedom, that is the evaluation at all vertices of the polygon, but is able to cope with a general polygon with N_V (straight or curved) edges.

We first focus on the case in which all edges are straight, and define the local VEM discrete space $\mathbf{V}_h(E)$ on a generic polygon E. Given the displacement values at each vertex, the virtual element function is first defined on the boundary, by a simple linear interpolation of the given vertex values on each edge. Thus the VEM space results to be a (globally continuous) piecewise polynomial of degree one on the boundary ∂E of the element. Afterward, in order to define the vector field on the whole element E, a typical choice is to assume that the virtual element space is (component-wise) harmonic inside E. That is, the functions $\boldsymbol{u}$ of the VEM space $\mathbf{V}_h(E)$ are required to satisfy $\Delta \boldsymbol{u} = \mathbf{0}$. It is well known that this leads to a uniquely well-defined function, given the boundary data, and such function will be continuous. In short:

$$\mathbf{V}_h(E) = \Big\{ \boldsymbol{u} \in [C^0(E)]^2 \ : \boldsymbol{u} \text{ is a first order polynomial on each edge,} \\ \Delta \boldsymbol{u} = \mathbf{0} \text{ inside the element} \Big\} .$$

Note that first order vector-valued polynomials are contained in $\mathbf{V}_h(E)$, and that in the case of triangles the original FEM space is recovered.

3.1.1. The curved edge case

In the presence of curved edges, the definition of the virtual element space needs to be modified, still keeping the same degrees of freedom as before (that is the evaluation of the displacements at the polygon vertices). We here follow the approach introduced in [50], while other possibilities [36,53] may be the topic of future work. Specifically, the first and main task is, for a given curved edge $e \in \partial E$ with assigned displacement values $\boldsymbol{u}(\nu)$, $\boldsymbol{u}(\nu')$ at its extrema ν, ν' (that correspond to element vertices), to reconstruct a displacement $\boldsymbol{u}$ on the whole curved edge. We therefore assume to have, as it happens for instance when the problem geometry is described in CAD, a (piecewise regular) parametrization of the curved boundary. By a simple restriction, this immediately yields a parametrization of each curved edge of any mesh element. Such parametrization will be an (invertible) mapping $\gamma : [a, b] \to e$, where $[a, b]$ denotes the parameter domain (an interval of the real line) and e the curvilinear mesh edge. The curvilinear space $\mathcal{S}_e$ is simply defined by the push forward of vector valued linear polynomials on e through the map γ, that is

$$\mathcal{S}_e = \left\{ \mathbf{v} : e \to \mathbb{R}^2 \mid \mathbf{v} = \mathbf{p} \circ \gamma^{-1} \text{ with } \mathbf{p} \in (\mathbb{P}_1[a, b])^2 \right\}$$

where $\mathbb{P}_1[a, b]$ denotes the space of first order polynomials on $[a, b]$. It can be checked that, if one applies the above definition to a straight edge and makes use of a standard linear parametrization, it returns the original "linear" interpolation. An example for the case of a circular edge is shown below.

When describing virtual functions $\boldsymbol{u}$ on a curved element E, the rest of the construction is the same as per the straight case. The vector field $\boldsymbol{u}$ is first defined on the boundary by using either the original "linear" interpolation (on straight edges) or the construction shown above (on curved edges). This allows to define the displacement $\boldsymbol{u}$ on the boundary ∂E, given the vertex displacement values. Then, $\boldsymbol{u}$ is extended inside the element by the same identical procedure as before (that is requiring $\Delta \boldsymbol{u} = \mathbf{0}$). In short:

$$\begin{aligned} \mathbf{V}_h(E) = \Big\{ \boldsymbol{u} \in [C^0(E)]^2 \ : & \boldsymbol{u} \text{ is a first order polynomial on each straight edge,} \\ & \boldsymbol{u} \in \mathcal{S}_e \text{ on each curved edge } e, \\ & \Delta \boldsymbol{u} = \mathbf{0} \text{ inside the element} \Big\} . \end{aligned}$$

Although the above space is not guaranteed to contain all "linear" polynomials, its approximation properties are as good as those of linear polynomials, as shown in [50].

We end the section with a short example, considering an edge e that is a circular segment with endpoints $\mathbf{X}_1$ and $\mathbf{X}_2$. Then, the circular segment can be parametrized by a map $\gamma : [a, b] \to \mathbb{R}^2$, $0 \le a < b < 2\pi$, that to each $\theta \in [a, b]$ associates the point of coordinates

$$\begin{cases} x = r \cos\theta + x_c \ , \\ y = r \sin\theta + y_c \ . \end{cases}$$

Here above the real numbers x_c, y_c, r are fixed once and for all (given the edge geometry), representing the coordinates (x_c, y_c) of the center of the circle and the radius r. Clearly $\gamma(a) = \mathbf{X}_1$ and $\gamma(b) = \mathbf{X}_2$. Since all computations (such as integrations along the edge) are computed in the parameter domain, the basis functions on the edge are described directly in terms of θ (in particular, note that one never needs to compute the inverse mapping γ^{-1}). As usual, let ϕ_1 and ϕ_2 represent the scalar basis functions associated, respectively, to the nodes $\mathbf{X}_1$ and $\mathbf{X}_2$. Then, since these are first order polynomials in the parameter θ (see the definition of $\mathcal{S}_e$), one simply obtains

$$\phi_1(\theta) = 1 - (\theta - a)/(b - a) \ , \qquad \phi_2(\theta) = (\theta - a)/(b - a) \ .$$

3.2. The VEM projection

Once the virtual space for curvilinear elements is defined, the rest of the construction is the same as for "standard" VEM with straight edges [22]. We describe it here briefly for completeness.

The first step is to introduce a representation of the local virtual space that can be computed, and we do so by introducing a projection Π on first order polynomials. Once one has this projection, the virtual function can be written as

$$\boldsymbol{u}_h = \Pi \boldsymbol{u}_h + (\boldsymbol{u}_h - \Pi \boldsymbol{u}_h) . \tag{13}$$

The range of Π is first order polynomials

$$\Pi \boldsymbol{u}_h = \mathbf{H}\mathbf{a} = \begin{bmatrix} 1 & 0 & x & 0 & y & 0 \\ 0 & 1 & 0 & x & 0 & y \end{bmatrix} \begin{bmatrix} a_1 \\ a_2 \\ \cdots \\ a_6 \end{bmatrix} \tag{14}$$

for every 2D element with the set of six unknown parameters $\mathbf{a}$. The goal is now to compute the set of parameters $\mathbf{a}$ as a map of the displacement values and thus the nodal degrees of freedom of a virtual element.

The computation of this polynomial function is based on the requirement that the gradient of the remainder $(\boldsymbol{u}_h - \Pi \boldsymbol{u}_h)$ is orthogonal to the gradient of any first order polynomial $\boldsymbol{u}_p$. This yields

$$\int_E \left[\nabla \boldsymbol{u}_p \cdot \nabla (\boldsymbol{u}_h - \Pi \boldsymbol{u}_h) \right] dE = 0 \,. \tag{15}$$

Since $\nabla \boldsymbol{u}_p = const.$ and $\nabla(\Pi \boldsymbol{u}_h) = const.$ (15) reduces to the condition that the gradients computed from the projected and real displacements must be equal

$$\int_E \nabla(\Pi \boldsymbol{u}_h) dE = \int_E \nabla \boldsymbol{u}_h \, dE \,. \tag{16}$$

While the left-hand-side is easily computable, the integral on the right-hand-side cannot be computed because $\boldsymbol{u}_h$ is not known within the element E. Therefore the integral on the right-hand side is transformed to a boundary integral

$$\nabla \Pi \boldsymbol{u}_h|_e = \frac{1}{|E|} \int_{\partial E} \boldsymbol{u}_h \otimes \boldsymbol{N} \, ds \tag{17}$$

where $\boldsymbol{N}$ is the outward normal to the element surface. For the two-dimensional case this results in

$$\begin{bmatrix} a_3 & a_5 \\ a_4 & a_6 \end{bmatrix} = \frac{1}{|E|} \sum_{k=1}^{N_V} \int_{e_k} \begin{bmatrix} u_x(s) N_x(s) & u_x(s) N_y(s) \\ u_y(s) N_x(s) & u_y(s) N_y(s) \end{bmatrix} \, ds \,, \tag{18}$$

where the left hand side is related to the gradient of $\Pi \boldsymbol{u}_h$ and the right hand side represents the edge by edge integration of $\boldsymbol{u}_h \otimes \boldsymbol{N}$. The symbol s represents a curvilinear coordinate along the edge, while N_x and N_y denote the components of the normal unit vector $\boldsymbol{N}$ (which will depend on s unless the edge is straight). Here $u_x(s)$ and $u_y(s)$ are the components of $\boldsymbol{u}_h$ defined at the boundary of the virtual element.

From this equation the parameters a_3 to a_6, representing the strain modes, can be found by simple comparison, see for instance [27,54]. For completeness of the polynomial in (14) the two parameters a_1 and a_2 have to be determined. They follow from the condition that the average vertex displacement value, when computed using the projection $\Pi \boldsymbol{u}_h$, has to be equal to the average vertex displacement value of the virtual function $\boldsymbol{u}_h$

$$\frac{1}{N_V} \sum_{i=1}^{N_V} \Pi \boldsymbol{u}_h(\boldsymbol{X}_i) = \frac{1}{N_V} \sum_{i=1}^{N_V} \boldsymbol{u}_h(\boldsymbol{X}_i) \,. \tag{19}$$

Now all kinematic quantities can be expressed in terms of the projection function. Hence, the symmetric strain tensor is the constant

$$\boldsymbol{\varepsilon} = \nabla_s \Pi \boldsymbol{u}_h|_e \,, \tag{20}$$

that can be interpreted as a computable approximation to $\nabla_s \boldsymbol{u}_h$.

Remark 1. The above construction requires to compute integrals on curved edges, that can be easily handled by mapping the curved edge to an interval of the real line (that is, using a parametrization of the edge) and applying standard 1D gauss integration. Moreover, the above formulas require the calculation of the area $|E|$ of curvilinear polygons E. This can be computed by directly applying some integration rule valid for curvilinear elements (see for instance [55,56]) or again reduced to a boundary integral by using an integration by parts.

3.3. Construction of the virtual element

Knowing the potential (12) and the kinematical quantities (20) a virtual element formulation can be derived as described in [27,54]. With the split in (13) the energy can be also split into a part governed by the deformation gradient of the projection and a stabilization part

$$U(\boldsymbol{u}) = \mathsf{A}_{k=1}^{N_E}[U_p(\Pi \boldsymbol{u}_h|_{E_k}) + U_{stab}(\boldsymbol{u}_h|_{E_k} - \Pi \boldsymbol{u}_h|_{E_k})] \,. \tag{21}$$

where A is the assembly operator. The energy contribution of each virtual element resulting from the displacement is found by inserting the VEM basis from into the potential (7)

$$U_p(\Pi \boldsymbol{u}_h) = \int_E [\,\Psi(\Pi \boldsymbol{u}_h) - \bar{\boldsymbol{f}} \cdot \Pi \boldsymbol{u}_h]\; dE - \int_{\partial E} \bar{\boldsymbol{t}} \cdot \Pi \boldsymbol{u}_h \; ds \,. \tag{22}$$

For the lowest order case here considered, the displacement gradient (20) is constant in E. However the parameters from (14) still depend on the displacement and thus the linear strain energy function in (5) leads to a linear equations system for the unknowns $\Pi \boldsymbol{u}_h$ that depend on the nodal degrees of freedom $\mathbf{u}_h|_e$ through Eqs. (18) and (19). Now the residual vector $\mathbf{R}_e^p$ and the stiffness matrix $\mathbf{K}_e^p$ can be computed at element level using U_p. This yields

$$\mathbf{R}_e^p = \frac{\partial U_p(\Pi \boldsymbol{u}_h)}{\partial \mathbf{u}_h|_e} \quad \text{and} \quad \mathbf{K}_e^p = \frac{\partial \mathbf{R}_e^p(\Pi \boldsymbol{u}_h)}{\partial \mathbf{u}_h|_e} \tag{23}$$

that are thus explicitly computable through $\mathbf{u}_h|_e$. Note however, that the contact area is not known a priori in contact mechanics. Hence the resulting equation system is nonlinear due to the inequality (10).

3.4. Stabilization of the method

A stabilization is needed since the range of the projection operator $\Pi \boldsymbol{u}_h$ can only cover the basic (first order polynomial) modes but not all the additional modes that stem for elements with more than 3 vertices. Different stabilization techniques can be employed; since the stabilization in presence of curved edges is identical to the straight-edge case we will limit ourselves to a brief description of some standard options.

3.4.1. Stabilizations directly based on the degrees of freedom

The easiest approach which was described in [22,27] is to introduce a pointwise error measure between the approximation function $\Pi \boldsymbol{u}_h(\boldsymbol{X}_I)$ and the real displacement values $\mathbf{u}_h|_I$ at node I:

$$d_u(\boldsymbol{X}_I) = [\mathbf{u}_h|_I - \Pi \boldsymbol{u}_h(\boldsymbol{X}_I)] \tag{24}$$

where $\mathbf{u}_h|_I$ are the nodal values at the **I**th vertex of the virtual element. When summed up over all element vertices N_V this leads to a stabilization term

$$U_{stab} = \frac{\gamma}{2} \sum_{I=1}^{N_V} [\mathbf{u}_h|_I - \Pi \boldsymbol{u}_h(\boldsymbol{X}_I)]^T [\mathbf{u}_h|_I - \Pi \boldsymbol{u}_h(\boldsymbol{X}_I)] \tag{25}$$

where the parameter is typically taken as

$$\gamma = \gamma_0 \frac{h_E^2 \; tr(\mathbb{D})}{tr(\mathbf{H}^T(\boldsymbol{X}_I)\mathbf{H}(\mathbf{X}_I))} \tag{26}$$

which includes the element diameter h_E as well as a part of the constitutive tensor $\mathbb{D}$. Here only the parameter γ_0 (that can be taken equal to 1) has to be chosen. This stabilization has the merit of being very simple and working well in many situations. Moreover it can be tuned to get a more robust behavior in the presence of volume locking, for instance by making the constant γ only dependent on the deviatoric part of the constitutive tensor. This element stabilization may lead to unphysical dents in the solution profile in the vicinity of nodes where vertices have a small distance to each other (in relation to the parent element size), see for instance [29].

A more advanced option was proposed in [36,57]

$$U_{stab} = \sum_{I=1}^{N_V} [\mathbf{u}_h|_I - \Pi \boldsymbol{u}_h(\boldsymbol{X}_I)]^T \; \mathbb{M} \; [\mathbf{u}_h|_I - \Pi \boldsymbol{u}_h(\boldsymbol{X}_I)] \tag{27}$$

where the ith term of the diagonal matrix $\mathbb{M}$ is the maximum among γ and the corresponding entry of the consistent stiffness matrix $\mathbf{K}_e^p$ in (23). This option often allows for a better accuracy, especially in cases where one is handling a complex local space (such as 3D problems and high order approximation degree) but does not cure the small-edge phenomena above.

A stabilization that cures the small-edge phenomena (sometimes at the price of a slightly worse overall accuracy) is the one proposed in [29]. This stabilization can still be described in the form (27), but with matrix in the form $\mathbb{M} = h_E \mathbb{Q}^T \mathbb{Q}$. Here the matrix $\mathbb{Q}$ corresponds to the first order finite difference matrix along the element boundary (for the details, see [29]). In such a way, the difference of displacement values at vertices that are very near (with respect to the parent element size) is strongly penalized.

3.4.2. Energy stabilization

The following approach [58] was introduced for the virtual element method in [54]. In contrast to the other stabilization methods this approach is based on the error in the resulting deformation energy rather than the error in just the displacement values. The strain energy U_p, see (21), is extended by a supplementary energy $\hat{U}$

$$U = U_p + \underbrace{\hat{U}(\boldsymbol{u}_h) - \hat{U}(\Pi \boldsymbol{u}_h)}_{U_{stab}} \tag{28}$$

so that for a convergent solution with very small elements $\hat{U}$ will cancel out, guaranteeing a consistent formulation. For coarser meshes the supplementary energy will work as a non-linear penalty term. The energy term related to the projected field $\Pi \boldsymbol{u}_h$ can be evaluated as in Section 3.3.

Since the contribution of $\boldsymbol{u}_h$ cannot be directly computed, a triangulation of the polygonal element is needed and a separate linear ansatz is used for every triangle. Note that this triangulation only uses the nodes that define the polygonal element, hence no extra degrees of freedom are introduced. Based on this ansatz the total energy in E is computed as the sum over the N_{int} internal triangles. In the presence of curved elements, one can simply first generate a standard straight-edge polygon E' by vertex-interpolation of the original curvilinear polygon E, and finally triangulate the element E'. Since stabilization need not to be accurate, substituting E with E' (but only when calculating the stabilization, not the consistent part) will not hinder the scheme performance.

Based on this ansatz the total energy in E is computed as the sum over the N_{int} internal triangles

$$\hat{U}(\mathbf{u}_h|_e) = \sum_{m=1}^{N_{int}} \int_{\Omega_m} \hat{\psi}(\boldsymbol{u}_h|_m)\, d\Omega\,. \tag{29}$$

The strain energy $\hat{\psi}$ can be freely selected. Here we use a Neo-Hookean material model with modified elastic Young's modulus $\hat{E}$ and Poisson's ratio $\hat{\nu}$ in order to optimize the element behavior, see [54] for the details. For the internal triangles linear ansatz functions are assumed, so that no numerical integration is necessary since all kinematical quantities in the sub-triangles are constant.

The last part in this stabilization procedure is the determination of the material parameters $\hat{E}$ and $\hat{\nu}$. As described by [59] and applied in [54] for virtual elements, the correction can be done to favor locking free and good bending behavior; we refer to such publications for an explicit expression of these two parameters.

4. Contact discretization

In computational contact mechanics exist many techniques to discretize the contact interface. In this work FEM and VEM will be compared. Two simple discretization strategies will be pursued: (i) Node-On-Segment, suitable for both FEM and VEM and (ii) Node-on-Node, where the advantage of VEM can be utilized for non-matching meshes at the contact interface:

– Node-to-Segment contact in which a node from body Ω^2 contacts a segment from the other body Ω^1. This is a classical contact discretization for non-matching meshes, see e.g. [1]. This approach is sketched in Fig. 2. In this case the integrals in (10) can be written as

$$U_c = \begin{cases} \int_{\Gamma_C} (\lambda_n + \frac{\epsilon_n}{2} g_n) g_n \, d\Gamma = \sum_{i=1}^{n_c} (\lambda_{n\,i} + \frac{\epsilon_n}{2} g_{n\,i}) g_{n\,i} \, A_i & \forall\, \lambda_{n\,i} \le 0 \quad \text{(contact)} \\ -\int_{\Gamma_C} \frac{1}{2\epsilon_n} \lambda_n^2 \, d\Gamma = \sum_{i=1}^{n_c} \frac{1}{2\epsilon_n} \lambda_{n\,i}^2 \, A_i & \forall \quad \lambda_{n\,i} > 0 \,\text{(separation)} \end{cases} \tag{30}$$

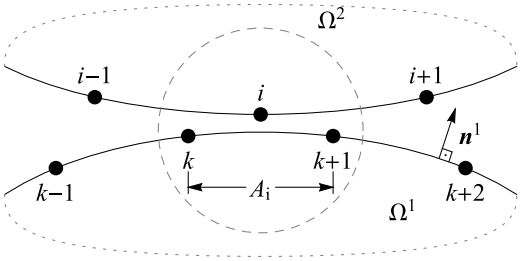

Fig. 2. Node to segment discretization.

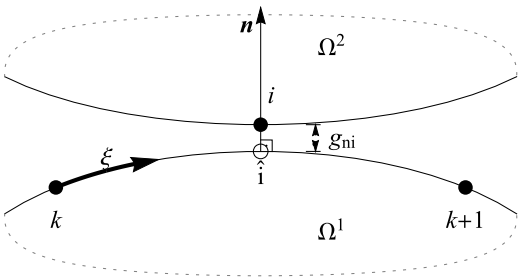

Fig. 3. Definition of the gap for node i.

where A_i is the area of the segment k–$(k+1)$ that is in contact with node i, see Fig. 2, and n_c denotes the total number of points being in contact. The gap $g_{n\,i}$ is then computed according to Fig. 3 as a difference between point of body Ω^2, $\boldsymbol{x}_i^2$, and its projection on body Ω^2, $\boldsymbol{x}_{\hat{i}}^1$. This leads to

$$g_{n\,i} = \left[\boldsymbol{x}_i^2 - \boldsymbol{x}_{\hat{i}}^1\right] \cdot \boldsymbol{n}^1 \tag{31}$$

The projection is defined as $\boldsymbol{x}_{\hat{i}} = \boldsymbol{x}^1(\bar{\xi})$, where $\bar{\xi}$ has to be found first. Depending on a case, the projection can usually be computed, by using a closest point projection onto the surface of body Ω^1 for node i which follows from:

$$\left[\boldsymbol{x}_i^2 - \boldsymbol{x}^1(\bar{\xi})\right] \cdot \boldsymbol{x}_{,\xi}^1(\bar{\xi}) = 0\,, \quad \text{where } \boldsymbol{x}_{,\xi}^1 = \frac{\partial \boldsymbol{x}^1}{\partial \xi}\,. \tag{32}$$

In general this is a nonlinear equation to be solved locally by Newton–Raphson method. For a line segment we have, $\boldsymbol{x}(\xi) = \boldsymbol{x}_k + \xi(\boldsymbol{x}_{k+1} - \boldsymbol{x}_k)$, and in case of a circular segment: $\boldsymbol{x}(\xi) = \boldsymbol{x}_C + r_C\{\cos(\phi_0 + \xi\,\Delta\phi), \sin(\phi_0 + \xi\,\Delta\phi)\}$, where ϕ_0 is angle of starting point and $\Delta\phi$ angle between starting and end point, $\boldsymbol{x}_C$ and r_C are centroid and radius of a circle.

– As another possibility for the contact discretization, node insertion can be applied to obtain a node-to-node or segment-to-segment contact. This is only possible in the case of virtual elements since these elements allow arbitrary numbers of nodes. This idea was presented first in [29] for geometrically linear problems using linear virtual elements and extended to nonlinear problem in [30] and is now adopted for contact problems with curved edges. In this case a projection scheme is employed that introduces nodes at the contact interface opposite to existing nodes and thus allows a node-to-node discretization of the contact interface, see e.g. [29] and Fig. 4. In this case the closest point procedure is used to define nodes on the opposite surfaces of the bodies. In Fig. 4 a new node $\hat{k}$ related to node k is introduced on the surface of Ω^2 as well as a new node $\hat{i}$ related to node i is introduced on the surface of Ω^1. The calculation of the projection is identical to node-on-segment, but instead here the projected node has to physically be inserted into the virtual element. This leads to a change in the element connectivity and number of degrees of freedom of the system. The discretization of node-to-node performed in similar manner to node-on-segment. The gap function (32) is used. Now the integral in (10) has to be evaluated for each node-to-node pair that is in contact. There are again two possibilities

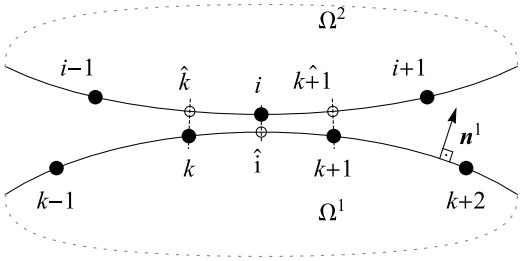

Fig. 4. Contact discretization using node insertion.

- The first one is a simple evaluation related to the contact points that yields equation (30), applied for each nodal pair at the contact interface, see Fig. 4 where n_c is now the total number of nodal pairs.
- The second evaluation of (10) needs a definition of the gap function and the Lagrangian parameters in one segment, e.g. the segment between nodes k and i with the pairs k–$\hat{k}$ and i–$\hat{i}$ and the length l_s. In this segment we can interpolate the Lagrangian parameter as

$$\lambda_{n\,s}(\xi) = [(1-\xi)\,\lambda_k + \xi\,\lambda_i] \tag{33}$$

and the gap function within this segment by

$$g_{n\,s}(\xi) = [(1-\xi)\,g_{n\,k} + \xi\,g_{n\,i}] \tag{34}$$

with ξ being the local coordinate that defines the segment ($0 \leq \xi \leq 1$).

$$U_c = \begin{cases} \int_{\Gamma_C} (\lambda_n + \frac{\epsilon_n}{2} g_n) g_n \, d\Gamma = \sum_{s=1}^{n_s} \int_0^1 (\lambda_{n\,s} + \frac{\epsilon_n}{2} g_{n\,s}) g_{n\,s}\, l_s d\xi & \forall\, \lambda_{n\,i} \leq 0 \quad \text{(contact)} \\ -\int_{\Gamma_C} \frac{1}{2\epsilon_n} \lambda_n^2 \, d\Gamma = \sum_{s=1}^{n_s} \int_0^1 \frac{1}{2\epsilon_n} \lambda_{n\,s}^2\, l_s d\xi & \forall \quad \lambda_{n\,i} > 0 \,\text{(separation)} \end{cases} \tag{35}$$

The integrals over the segments can be evaluated exactly for the interpolation in (33) and (34). This leads to

$$\int_0^1 (\lambda_{n\,s} + \frac{\epsilon_n}{2} g_{n\,s}) g_{n\,s}\, l_s d\xi = \frac{l_s}{6} \left[\varepsilon_n (g_{nk}^2 + g_{nk} g_{ni} + g_{ni}^2) + (2\lambda_k + \lambda_i) g_{nk} + (\lambda_k + 2\lambda_i) g_{ni} \right] \tag{36}$$

and

$$\int_0^1 \frac{1}{2\epsilon_n} \lambda_{n\,s}^2\, l_s d\xi = \frac{l_s}{6\epsilon_n} (\lambda_k^2 + \lambda_k \lambda_i + \lambda_i^2) \tag{37}$$

Both discretization schemes are employed in this contribution, although only the first option of node-to-node contact was used in the shown examples. Differences in the results are shown in the following examples.

5. Numerical examples

We now demonstrate the performance of the proposed virtual element formulation for curved edges with applications to contact mechanics by means of three representative numerical examples. For comparison purposes, results of the standard finite element method are also demonstrated. The results are very promising and underline the advantages of the new VEM formulation for contact between two elastic bodies in the presence of curved interfaces.

In general the following mesh discretizations will be analyzed:

– FEM-STR: standard first order FE mesh with 4 noded quadrilateral elements.
– VEM-STR: regular VEM mesh with 4 noded quadrilateral elements.
– VEM-STRr: locally refined VEM-STR element.
– VEM-VRN: Voronoi cell mesh with arbitrary number of element nodes.

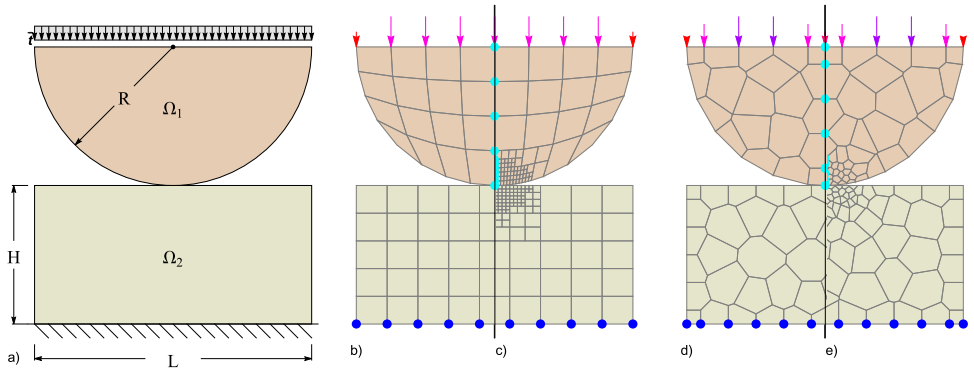

Fig. 5. Hertzian contact problem. (a) Geometry and boundary conditions; (b) structured 4 node quadrilateral discretization (STR); (c) Refined structured mesh (STR-ref) and (d) Voronoi cell mesh (VRN); (e) Refined Voronoi cell mesh (VRN-ref).

– VEM-VRNr: locally refined VEM-VRN element.

These listed cases will be analyzed for both described stabilization types: sub-triangulation (Stab. A) introduced in [38], see Section 3.4.2; and algebraic stabilization (Stab. B) developed in [22,27], see (25). Additionally the following contact types of Section 4 will be discussed:

– SN ln-ln: standard node to segment contact (Line-to-Line), where both edges are assumed linear,
– SN ln-crv standard node to segment contact (Line-to-Curve), where one edge (e.g. disk in the first example) is assumed curved,
– NN ln-crv node on node contact (Line-to-Curve), where disk edge is assumed curved. Due to node insertion, this type can only be performed on VEM,

where the nodes are projected from Ω_1 to Ω_2 and opposite.

The locally-refined structured meshes are refined until elements within the predefined contact area refined $n_{ref} \in (1, 2, 3, 4)$ times. Whereas the locally-refined Voronoi mesh is based on the refinement until elements in the contact area of mesh have an area below $|\bar{\Omega}_e|/n_{ref}^2$, where $|\bar{\Omega}_e|$ is average element size of non-refined Voronoi mesh.

5.1. Hertzian contact problem

The first example is the elastic contact between a disk Ω_1 and a nearly rigid block Ω_2, representing the so-called Hertzian contact problem. It is a well-known benchmark test in contact mechanics due to the existence of an analytical solution (AS) to verify the contact discretization. In line with [60], the analytical solution of the contact pressure p_n over the contact area is given by

$$p_n = \frac{4R\,\bar{t}}{\pi b^2}\sqrt{b^2 - x^2} \quad \text{with} \quad b = 2\sqrt{\frac{2R^2\,\bar{t}}{\pi E^*}} \quad \text{and} \quad \frac{1}{E^*} = \frac{1-\nu_1^2}{E_1} + \frac{1-\nu_2^2}{E_2} \tag{38}$$

Hence, this solution can be compared with the results obtained by the virtual element method VEM.

The geometrical setup and the loading conditions of the contact problem are depicted in Fig. 5(a). The block length is chosen to be $L = 20$ and height is $H = 10$, whereas the disk radius is set to $R = 10$. On the lower half of the disk we apply a uniform line load of magnitude $\bar{t} = 25$ hence the total load is 500 as shown in Fig. 5(a). The elastic material parameters are chosen as $E_1 = 7000$, $E_2 = 70000$ and $\nu_1 = \nu_2 = 0.3$. Using the above described set of parameters, the maximum contact pressure yields $p_{n,max} = 333.61$ and the contact width is $b = 0.954$ which will be compared with numerical solution.

Fig. 6 demonstrates the stress distribution σ_{yy} for different mesh discretization. As a reference model, we used the refined finite element mesh in Fig. 6(b). Here similar results were observed for all VEM and FEM elements. In order to investigate the virtual element performance, a comparison with the analytical solution is performed. To this end, in Fig. 7 a complete convergence study where various meshes and three contact schemes, namely: Line-to-Line

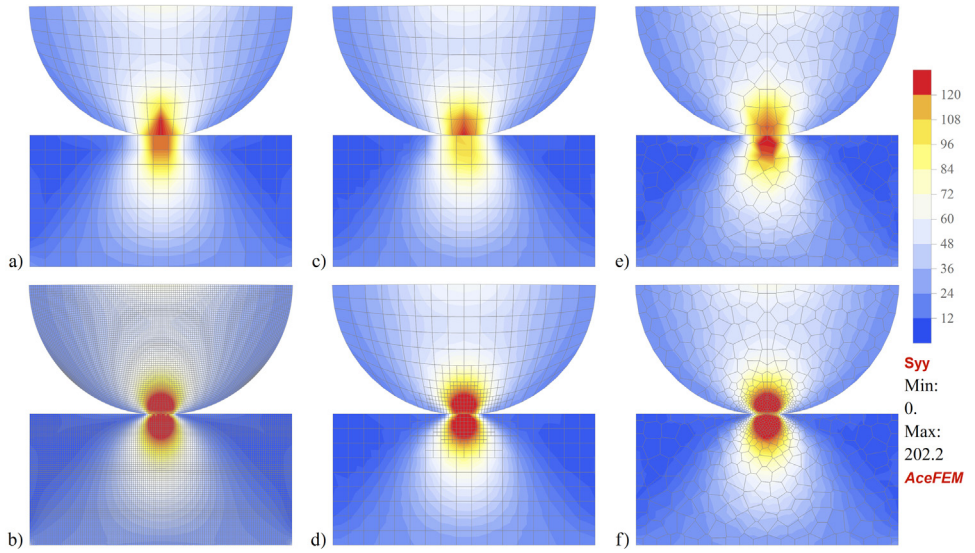

Fig. 6. Hertzian contact problem — Stress distribution σ_{yy} for node on curved segment contact case (SN: ln-crv): (a) Standard FEM-STR; (b) fine FEM-STR (overkill solution); (c) Standard VEM-STR; (d) local refined VEM-STRr; (e) coarse VRN mesh and (f) local refined VRNr mesh.

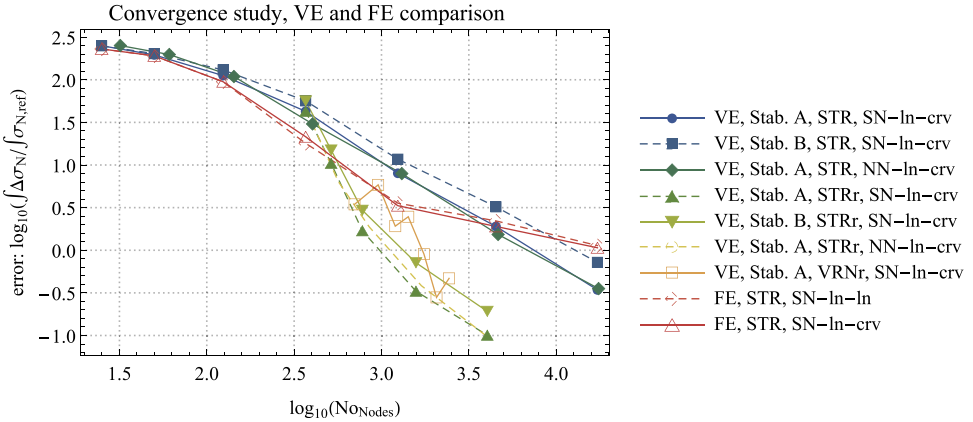

Fig. 7. Hertzian contact problem – convergence study – the error between example and analytical solution (AS).

and Line-to-Curve contact techniques for node to segment and node to node for VEM with both stabilization. The convergence study shows the error between analytical curve and numerical curves. As expected a linear convergence behavior is achieved in the simulations. Moreover, we observe that all types of contact schemes yield similar results (Fig. 7) which converge to the analytical solution with increasing the mesh refinements. Furthermore, both analyzed stabilization techniques, lead to a good agreement with the analytical solutions for finer meshes as shown in Fig. 8, where for finest refinement the graphs coincide, except FEM solution for the same number of mesh divisions $\boldsymbol{n}_{div} = 6$, which reruns slightly overestimated stresses, however Stabilization A returns lower errors. Note that the local refinement of the mesh around the contact area produce similar results to the fully refined meshes, yet with less degrees of freedoms, as illustrated in Fig. 9 and can also be observed at the convergence plot (Fig. 7). The significant deviation of the FEM solution from the maximal AS contact pressure can be resolved by further mesh refinement, as demonstrated in Fig. 9b for $\boldsymbol{n}_{div} = 9$.

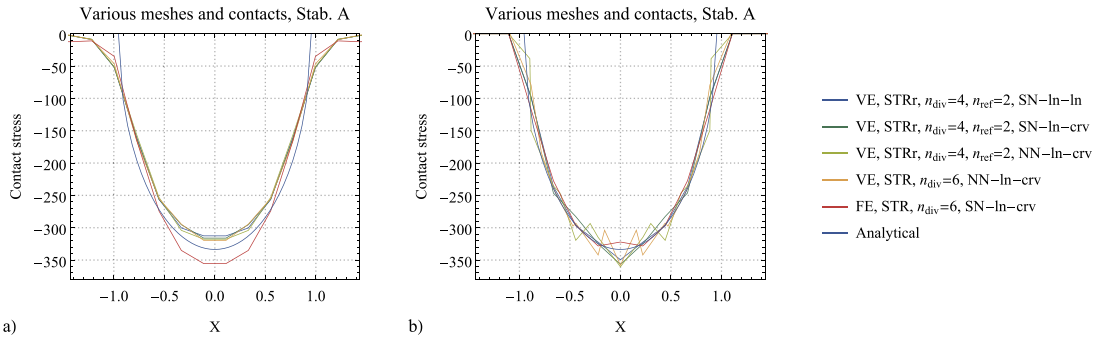

Fig. 8. Hertzian contact problem — Stress distribution in normal direction over the contact zone for various VEM compared with FEM and analytical solution for Stabilization A. The stresses obtained from actual stress on surface as $\sigma_n = (\boldsymbol{\sigma}\,\boldsymbol{n}) \cdot \boldsymbol{n}$ are shown in (a) and the stresses obtained by normalization of contact element residuals as $\sigma_n = (\boldsymbol{R}_c/A_c) \cdot \boldsymbol{n}$ are shown in (b).

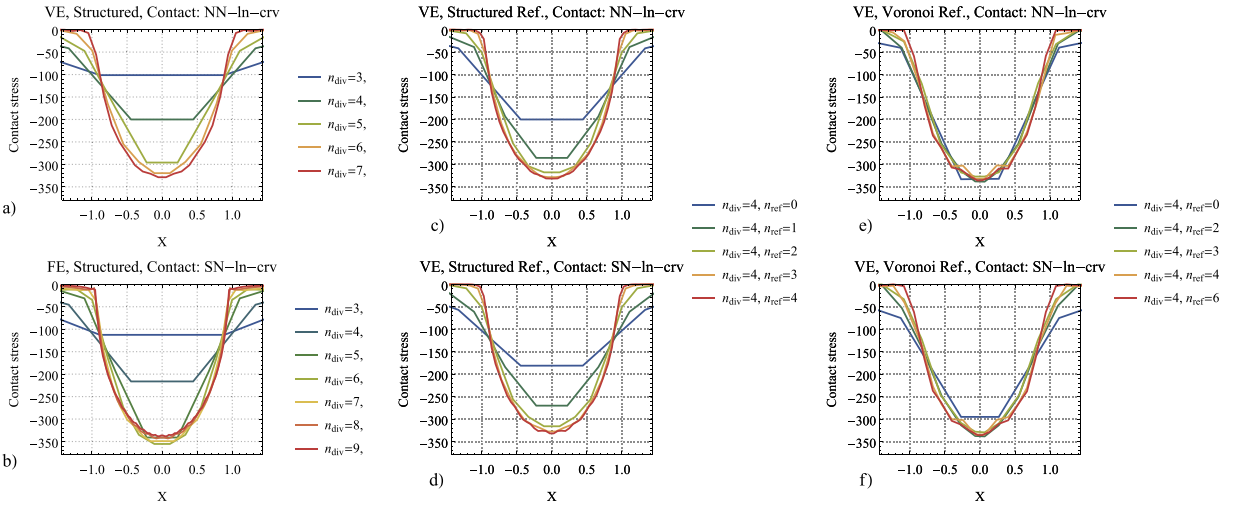

Fig. 9. Hertzian contact problem — Stress distribution in normal direction over the contact zone defined as $\sigma_n = (\boldsymbol{\sigma}\,\boldsymbol{n}) \cdot \boldsymbol{n}$ for Node-to-Curve-Contact of VEM-STR in (a); refined VEM-STRr in (c, d); refined VEM-VRNr (e, f). Graphs (a, c, e) belong to Stabilization A and graphs (d, f) for Stabilization B. Whereas, the FEM solution is given in (b).

5.2. *Beams in contact*

In the second example we study the contact among two beams. The two beams are clamped on one side and in contact on the other side. The setup and loading are shown in Fig. 10(a). The beam sizes are: $H_1 = H_2 = 1$, $L_1 = L_2 = 20$ and $R = 2$. A uniform line load is applied on top of the free end of the upper beam Ω_1 with magnitude $\bar{t} = 50$, as illustrated in Fig. 10(a). The elastic material parameters are selected as $E_1 = E_2 = 70000$ and $\nu_1 = \nu_2 = 0.3$. Four different VEM mesh types are investigated to illustrate the performance of the virtual element method under bending and contact deformations, as demonstrated in Fig. 10(b–e) and are compared with FEM on a structured quadrilateral mesh as shown in Fig. 10(d).

Fig. 12 depicts the distribution of the von Mises stress σ_{VM} for the four different elements in Fig. 10. All elements give similar results and are in agreement with the overkilling solution.

Another goal here is to illustrate the performance of the stabilization techniques of the virtual element method in a contact problem for thin bending state. To this end, Fig. 11 shows a convergence study for the displacement at the top left corner point of Ω_1 versus mesh refinements. We observe that all schemes converge to the benchmark solution obtained with the overkilling mesh. The stabilization based on the sub-triangulation (A) yields more accurate results for this thin beam bending problem as documented in [29,38]. In this example, no major difference between contact techniques was observed.

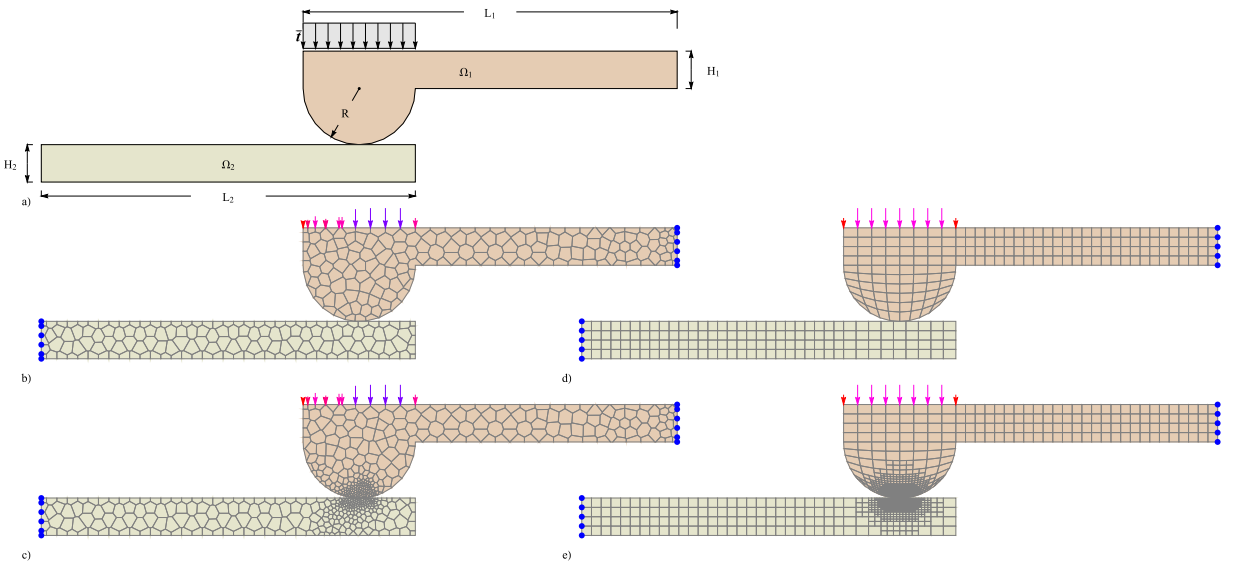

Fig. 10. Beams in contact. (a) Geometry and boundary conditions; (b) Voronoi mesh (VRN); (c) locally refined Voronoi mesh (VRNr); (d) structured (STR) mesh; and (e) locally refined structured mesh (STRr).

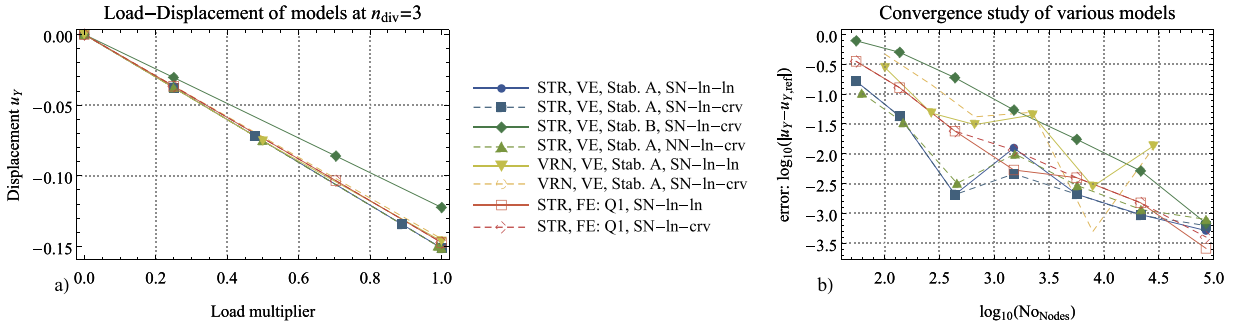

Fig. 11. Beams in contact — convergences study. Comparison between different meshes, contact schemes and stabilizations. Overkill FEM structured solution was used as a reference displacement $u_{y,ref}$.

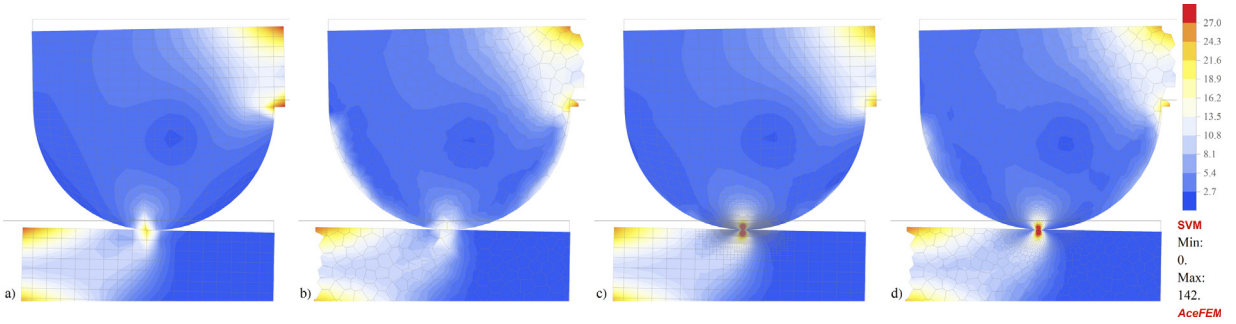

Fig. 12. Beams in contact — von Mises stress σ_{VM} distribution. (a) Uniform FEM-STR; (b) uniform VEM-VRN and (c) local refined VEM-STRr; (d) local refined VEM-VRNr.

Possibly, the performance of stabilization (B) with respect to thin bending problems (such as the present one) could be improved by devising a stability parameter γ (see (25)) that takes also into account the aspect ratio of the element; such investigation is outside the focus of the present work.

5.3. Circular joint contact

In the last example, the elastic contact between two circular objects are analyzed. The aim of this test is to illustrate the benefits of using curved virtual elements in comparison with the standard VEM approach with straight edges. Hence both bodies are curved at the contact zone to check the performance of the proposed formulations. Fig. 13(a) depicts the geometry, boundary conditions and loading of the joint contact. Hereby the lower block Ω_2 is fixed at the outer straight boundaries in the normal direction. A distributed load, as a vertical force of total value $F_y = 2500$, is applied at the top of the circular body Ω_1, as illustrated in Fig. 13(a) with magnitude of $\bar{t} \approx -400$ since the load width depends on the actual mesh. The block Ω_2 length is chosen to be $L = 40$, height is $H = 20$ and the radius of block curvature is $R_{OUT} = 10.05$ and radius of the disk is $R_{IN} = 10$. The circles touch at the bottom point. We employ four different virtual element meshes and compare their results with the FEM solution. The contact pressure on the two bodies is plotted with blue and green colors in Fig. 14.

Fig. 15 demonstrates the von Mises stress distribution σ_{VM} for different mesh discretizations. We observe similar results for all VEM meshes and curved contact discretizations, in good agreement with the reference solution obtained with an overkilling mesh. To illustrate the advantage of using a curved-to-curved virtual element contact formulation, as opposed to a line-to-line approach, Fig. 16 compares different discretization techniques for all contact schemes. Here, one clearly observes the oscillation of the contact normal stress for all elements when making use of the line-to-line contact scheme, see Fig. 16(a, b). The meshes in line-to-line contact will interpenetrate each other already in initial configuration, producing additional stresses, while they should be stress-free-state. On the contrary, the curve-to-curve contact VEM scheme yields significantly smoother contact pressure patterns, as

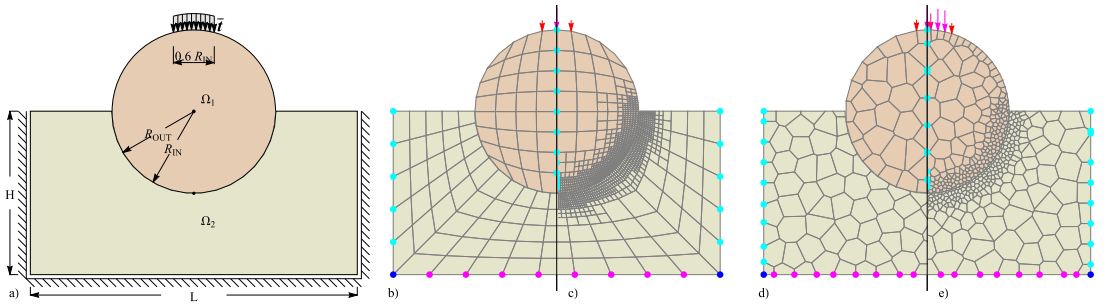

Fig. 13. Circular joint contact. (a) Geometry and boundary conditions; (b) FEM/VEM-STR uniform discretization; (c) local refined VEM-STRr (d) VEM-VRN with Voronoi cell mesh; and (e) local refined VEM-VRNr mesh.

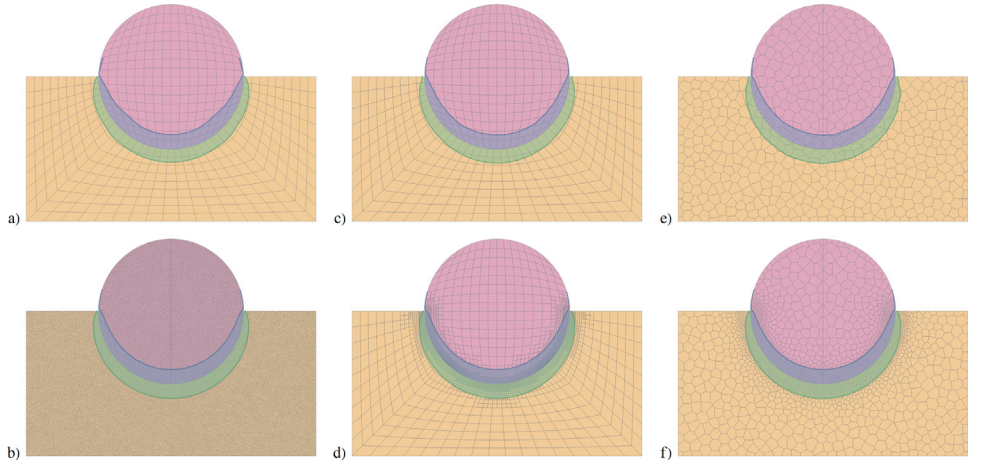

Fig. 14. Circular joint contact — color plot for contact pressure distribution: (a) Uniform FEM-Q1 mesh; (b) fine VEM-VRN; (c) uniform VEM-STR mesh; (d) refined VEM-STRr mesh; (e) VEM-VRN mesh and (f) refined VEM-VRNr mesh.

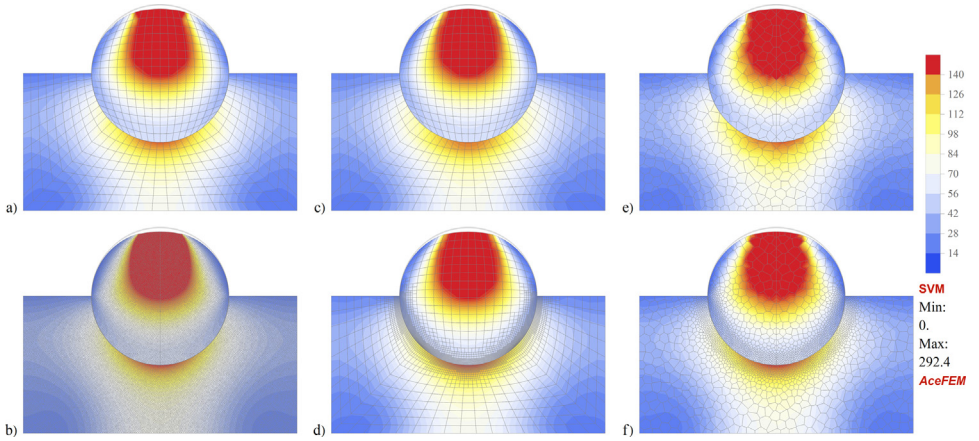

Fig. 15. Circular joint contact — Stress distribution σ_{VM}. (a) Standard FEM-STR; (b) fine VEM-VRN; (c) regular VEM-STR; (d) locally refined VEM-STRr; (e) coarse VEM-VRN mesh and (f) locally refined VEM-VRNr mesh.

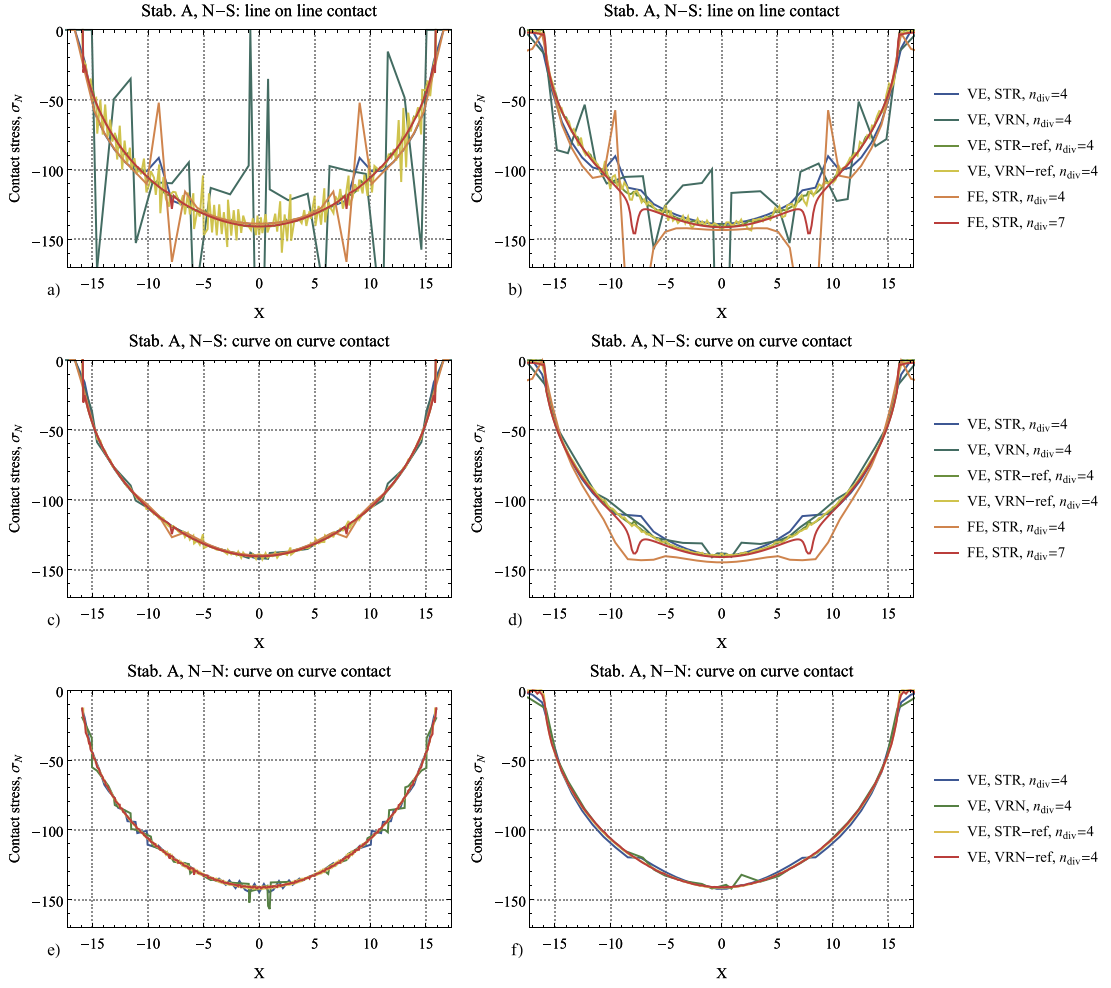

Fig. 16. Circular joint contact — contact normal stress over the contact zone: Line-to-Line-Contact in (a, b), Curve-to-Curve contact in (c, d) and Node-to-Node with Curve-to-Curve contact in (e, f) for stabilization A and different mesh discretizations. Stresses obtained by normalization of contact element residuals as $\sigma_n = (\boldsymbol{R}_c/A_c)\cdot\boldsymbol{n}$ are shown in (a, c, e) and stresses obtained from actual stress on surface as $\sigma_n = (\boldsymbol{\sigma}\,\boldsymbol{n})\cdot\boldsymbol{n}$ are shown in (b, d, f).

shown in Fig. 16(c–f). Furthermore, note that in this test the (A) and (B) stabilizations produce very similar results. Both Node-to-Node and Node-to-Curved Segment contact formulations produce similar results. However the former produces better stress distribution, where stresses are obtained from actual element stresses (Fig. 16)(b, d, f), while latter produces better stress distribution when stresses are obtained from normalization of residual (Fig. 16)(a, c, e), where it is observable that the oscillations are present due to unknown contributing areas.

As a final remark, we note that one may apply typical smoothing techniques in order to improve both schemes accuracy.

6. Conclusion

A virtual element scheme for curved edges with applications to contact mechanics was outlined within this work. In VEM, arbitrary shaped elements with a number of nodes in an element can be changed easily during the simulation process. Here we used a non-matching mesh at interfaces, hence avoid the need for node-to-node contact. In this work, the recently developed VEM technology for contact mechanics was further extended towards curved edges to account for exact approximation of complex geometries at interfaces. It was noted that a curvilinear implementation does not imply any significant complication with respect to standard VEM methodology. Furthermore, it can be implemented into existing codes quite easily. Numerical results were very promising and indicate the proposed curvilinear VEM as a viable and competitive technology for contact between curved surfaces. Throughout the paper edges with constant curvature (i.e. circle) were considered, however the method can be generalized to any parametrizable curve.

Declaration of competing interest

The authors declare that they have no known competing financial interests or personal relationships that could have appeared to influence the work reported in this paper.

Acknowledgments

The authors F. Aldakheel and P. Wriggers gratefully acknowledge support for this research by the “German Research Foundation” (DFG) in (i) the COLLABORATIVE RESEARCH CENTER **CRC 1153** and (ii) the PRIORITY PROGRAM **SPP 2020** within their second funding phases. The author L. Beirao da Veiga was partially supported by the EUROPEAN RESEARCH COUNCIL through the **H2020** Consolidator Grant (Grant No. 681162) CAVE, Challenges and Advancements in Virtual Elements, and by the MIUR, Italy through the PRIN Grant No. 201744KLJL (this support is gratefully acknowledged). The author E. Artioli gratefully acknowledges the partial financial support of **PRIN 2017**, Italy project “3D Printing: a bridge to the future (3DP_Future). Computational methods, innovative applications, experimental validations of new materials and technologies”, grant 2017L7X3CS_004.

References

[1] P. Wriggers, Computational Contact Mechanics, second ed., Springer, Berlin, Heidelberg, New York, 2006.
[2] T.A. Laursen, Computational Contact and Impact Mechanics, Springer, Berlin, New York, Heidelberg, 2002.
[3] J.O. Hallquist, NIKE2d: An Implicit, Finite-Deformation, Finite Element Code for Analysing the Static and Dynamic Response of Two-Dimensional Solids, Tech. Rep. UCRL–52678, University of California, Lawrence Livermore National Laboratory, 1979.
[4] P. Wriggers, J. Simo, A note on tangent stiffnesses for fully nonlinear contact problems, Commun. Appl. Numer. Methods 1 (1985) 199–203.
[5] J.O. Hallquist, G.L. Goudreau, D.J. Benson, Sliding interfaces with contact-impact in large-scale Lagrange computations, Comput. Methods Appl. Mech. Engrg. 51 (1985) 107–137.
[6] G. Pietrzak, A. Curnier, Continuum mechanics modeling and augmented Lagrange formulation of multibody, large deformation frictional contact problems, in: D.R. Owen, E. Hinton, E. Onate (Eds.), Proceedings of COMPLAS 5, CIMNE, Barcelona, 1997, pp. 878–883.
[7] V. Padmanabhan, T. Laursen, A framework for development of surface smoothing procedures in large deformation frictional contact analysis, Finite Elem. Anal. Des. 37 (2001) 173–198.
[8] P. Wriggers, L. Krstulovic-Opara, J. Korelc, Smooth C^1- interpolations for two-dimensional frictional contact problems, Internat. J. Numer. Methods Engrg. 51 (2001) 1469–1495.
[9] L. Krstulovic-Opara, P. Wriggers, J. Korelc, A C^1-continuous formulation for 3D finite deformation frictional contact, Comput. Mech. 29 (2002) 27–42.
[10] I. Temizer, P. Wriggers, T.J.R. Hughes, Contact treatment in isogeometric analysis with nurbs, Comput. Methods Appl. Mech. Engrg. 200 (2011) 1100–1112.

[11] L. de Lorenzis, P. Wriggers, G. Zavarise, Isogeometric analysis of 3D large deformation contact problems with the augmented Lagrangian formulation, Comput. Mech. 49 (2012) 1–20.
[12] L. de Lorenzis, I. Temizer, P. Wriggers, G. Zavarise, A large deformation frictional contact formulation using NURBS-based isogeometric analysis, Internat. J. Numer. Methods Engrg. 87 (2011) 1278–1300.
[13] I. Temizer, P. Wriggers, T.J.R. Hughes, Three-dimensional mortar-based frictional contact treatment in isogeometric analysis with nurbs, Comput. Methods Appl. Mech. Engrg. 209–211 (2012) 115–128.
[14] A. Popp, M.W. Gee, W.A. Wall, A finite deformation mortar contact formulation using a primal–dual active set strategy, Internat. J. Numer. Methods Engrg. 79 (11) (2009) 1354–1391.
[15] T.A. Laursen, M.A. Puso, J. Sanders, Mortar contact formulations for deformable–deformable contact: past contributions and new extensions for enriched and embedded interface formulations, Comput. Methods Appl. Mech. Engrg. 205 (2012) 3–15.
[16] B. Wohlmuth, R. Krause, Monotone methods on non-matching grids for non linear contact problems, SISC 25 (2004) 324–347.
[17] K.A. Fischer, P. Wriggers, Frictionless 2D contact formulations for finite deformations based on the mortar method, Comput. Mech. 36 (2005) 226–244.
[18] K.A. Fischer, P. Wriggers, Mortar based frictional contact formulation for higher order interpolations using the moving friction cone, Comput. Methods Appl. Mech. Engrg. 195 (2006) 5020–5036.
[19] M. Tur, F. Fuenmayor, P. Wriggers, A mortar-based frictional contact formulation for large deformations using Lagrange multipliers, Comput. Methods Appl. Mech. Engrg. 198 (2009) 2860–2873.
[20] N. Noii, F. Aldakheel, T. Wick, P. Wriggers, An adaptive global–local approach for phase-field modeling of anisotropic brittle fracture, Comput. Methods Appl. Mech. Engrg. 361 (2020) 112744.
[21] F. Aldakheel, N. Noii, T. Wick, P. Wriggers, A global-local approach for hydraulic phase-field fracture in poroelastic media, Comput. Math. Appl. (2020) http://dx.doi.org/10.1016/j.camwa.2020.07.013.
[22] L. Beirão da Veiga, F. Brezzi, A. Cangiani, G. Manzini, L.D. Marini, A. Russo, Basic principles of virtual element methods, Math. Models Methods Appl. Sci. 23 (1) (2013) 199–214.
[23] L. Beirão da Veiga, F. Brezzi, L.D. Marini, A. Russo, The hitchhiker's guide to the virtual element method, Math. Models Methods Appl. Sci. 24 (08) (2014) 1541–1573.
[24] P. Wriggers, F. Aldakheel, B. Hudobivnik, Application of the Virtual Element Method in Mechanics, GAMM-Rundbriefe, 2019, pp. 4–10.
[25] L. Beirão da Veiga, F. Brezzi, L.D. Marini, Virtual elements for linear elasticity problems, SIAM J. Numer. Anal. 51 (2) (2013) 794–812.
[26] A.L. Gain, C. Talischi, G.H. Paulino, On the virtual element method for three-dimensional linear elasticity problems on arbitrary polyhedral meshes, Comput. Methods Appl. Mech. Engrg. 282 (2014) 132–160.
[27] E. Artioli, L. Beirão da Veiga, C. Lovadina, E. Sacco, Arbitrary order 2D virtual elements for polygonal meshes: Part I, elastic problem, Comput. Mech. 60 (3) (2017) 355–377.
[28] E. Artioli, S. de Miranda, C. Lovadina, L. Patruno, A stress/displacement virtual element method for plane elasticity problems, Comput. Methods Appl. Mech. Engrg. 325 (2017) 155–174.
[29] P. Wriggers, W.T. Rust, B.D. Reddy, A virtual element method for contact, Comput. Mech. 58 (6) (2016) 1039–1050.
[30] P. Wriggers, W.T. Rust, A virtual element method for frictional contact including large deformations, Eng. Comput. 36 (7) (2019) 2133–2161.
[31] B. Hudobivnik, F. Aldakheel, P. Wriggers, A low order 3D virtual element formulation for finite elasto–plastic deformations, Comput. Mech. 63 (2) (2019) 253–269.
[32] F. Aldakheel, B. Hudobivnik, P. Wriggers., Virtual elements for finite thermo-plasticity problems, Comput. Mech. 64 (5) (2019) 1347–1360.
[33] E. Artioli, L. Beirao da Veiga, C. Lovadina, E. Sacco, Arbitrary order 2D virtual elements for polygonal meshes: Part II, inelastic problem, Comput. Mech. 60 (2017) 643–657.
[34] P. Wriggers, B. Hudobivnik, J. Schröder, Finite and Virtual Element Formulations for Large Strain Anisotropic Material with Inextensive Fibers, Springer International Publishing, Cham, 2018, pp. 205–231.
[35] B.D. Reddy, D. van Huyssteen, A virtual element method for transversely isotropic elasticity, Comput. Mech. (2019) http://dx.doi.org/10.1007/s00466-019-01690-7.
[36] E. Artioli, L. Beirão da Veiga, F. Dassi, Curvilinear virtual elements for 2D solid mechanics applications, Comput. Methods Appl. Mech. Engrg. 359 (2020) 112667.
[37] H. Chi, L. Beirão da Veiga, G. Paulino, Some basic formulations of the virtual element method (VEM) for finite deformations, Comput. Methods Appl. Mech. Engrg. 318 (2017) 148–192.
[38] P. Wriggers, B. Reddy, W. Rust, B. Hudobivnik, Efficient virtual element formulations for compressible and incompressible finite deformations, Comput. Mech. 60 (2017) 253–268.
[39] A. Hussein, F. Aldakheel, B. Hudobivnik, P. Wriggers, P.-A. Guidault, O. Allix, A computational framework for brittle crack-propagation based on efficient virtual element method, Finite Elem. Anal. Des. 159 (2019) 15–32.
[40] F. Aldakheel, B. Hudobivnik, A. Hussein, P. Wriggers, Phase-field modeling of brittle fracture using an efficient virtual element scheme, Comput. Methods Appl. Mech. Engrg. 341 (2018) 443–466.
[41] F. Aldakheel, B. Hudobivnik, P. Wriggers, Virtual element formulation for phase-field modeling of ductile fracture, Int. J. Multiscale Comput. Eng. 17 (2) (2019) 181–200.
[42] E. Artioli, S. Marfia, E. Sacco, Vem-based tracking algorithm for cohesive/frictional 2D fracture, Comput. Methods Appl. Mech. Engrg. 365 (2020) 112956.

[43] F. Aldakheel, A microscale model for concrete failure in poro-elasto-plastic media, Theor. Appl. Fract. Mech. 107 (2020) 102517.
[44] A. Gain, G. Paulino, S. Leonardo, I. Menezes, Topology optimization using polytopes, Comput. Methods Appl. Mech. Engrg. 293 (2015) 411–430.
[45] K. Park, H. Chi, G.H. Paulino, On nonconvex meshes for elastodynamics using virtual element methods with explicit time integration, Comput. Methods Appl. Mech. Engrg. 356 (2019) 669–684.
[46] K. Park, H. Chi, G.H. Paulino, Numerical recipes for elastodynamic virtual element methods with explicit time integration, Internat. J. Numer. Methods Engrg. 121 (1) (2020) 1–31.
[47] M. Cihan, F. Aldakheel, B. Hudobivnik, P. Wriggers, Virtual element formulation for finite strain elastodynamics, 2020, arXiv preprint arXiv:2002.02680.
[48] E. Artioli, Asymptotic homogenization of fibre-reinforced composites: a virtual element method approach, Meccanica 53 (2018) 1187–1201.
[49] P. Wriggers, B. Hudobivnik, F. Aldakheel, A virtual element formulation for general element shapes, Comput. Mech. (2020) http://dx.doi.org/10.1007/s00466-020-01891-5.
[50] L. Beirão da Veiga, A. Russo, G. Vacca, The virtual element method with curved edges, ESAIM: M2AN 53 (2) (2019) 375–404.
[51] E. Artioli, L. Beirão da Veiga, M. Verani, An adaptive curved virtual element method for the statistical homogenization of random fibre-reinforced composites, Finite Elem. Anal. Des. 177 (2020) 103418.
[52] J. Lengiewicz, J. Korelc, S. Stupkiewicz, Automation of finite element formulations for large deformation contact problems, Internat. J. Numer. Methods Engrg. 85 (10) (2011) 1252–1279.
[53] L. Beirão da Veiga, F. Brezzi, L.D. Marini, A. Russo, Polynomial preserving virtual elements with curved edges, Math. Mod. and Meth. in Appl. Sci. (2020) http://dx.doi.org/10.1142/S0218202520500311.
[54] P. Wriggers, B. Reddy, W. Rust, B. Hudobivnik, Efficient virtual element formulations for compressible and incompressible finite deformations, Comput. Mech. 60 (2) (2017) 253–268.
[55] A. Sommariva, M. Vianello, Gauss-Green cubature and moment computation over arbitrary geometries, J. Comput. Appl. Math. 231 (2009) 886–896.
[56] E. Artioli, A. Sommariva, M. Vianello, Algebraic cubature on polygonal elements with a circular edge, Comput. Math. Appl. 79 (2020) 2057–2066.
[57] L. Beirão da Veiga, F. Dassi, A. Russo, High-order virtual element method on polyhedral meshes, Comput. Math. Appl. 74 (5) (2017) 1110–1122.
[58] P. Krysl, Mean-strain eight-node hexahedron with stabilization by energy sampling, Internat. J. Numer. Methods Engrg. 102 (3–4) (2015) 437–449.
[59] P. Krysl, Mean-strain 8-node hexahedron with optimized energy-sampling stabilization, Finite Elem. Anal. Des. 108 (2016) 41–53.
[60] K.L. Johnson, Contact Mechanics, Cambridge University Press, 1985.